

SUPPLEMENTARY MATERIAL

Orientation selection in distance measurements between nitroxide spin labels at 94 GHz EPR with variable frequency separation

Igor Tkach¹, Soraya Pornsuwan¹, Claudia Höbartner², Falk Wachowius², Snorri Th. Sigurdsson³, Tatiana Baranova⁴, Ulf Diederichsen⁴, Giuseppe Sicoli¹ & Marina Bennati^{1,4,*}

¹Max Planck Institute for Biophysical Chemistry, EPR Spectroscopy Group, Göttingen, Germany. ²Max Planck Institute for Biophysical Chemistry, Nucleic Acid Chemistry Group, Göttingen, Germany. ³University of Iceland, Department of Chemistry, Science Institute, Reykjavik, Iceland. ⁴University of Göttingen, Department of Organic and Biomolecular Chemistry, Germany.

S1. 9-GHz PELDOR experiments of RNA duplex

S2. 9-GHz PELDOR experiments of the TOPP-labeled peptide

S3. Data analysis

S4. Effect of libration of the TOPP label around its internal axes.

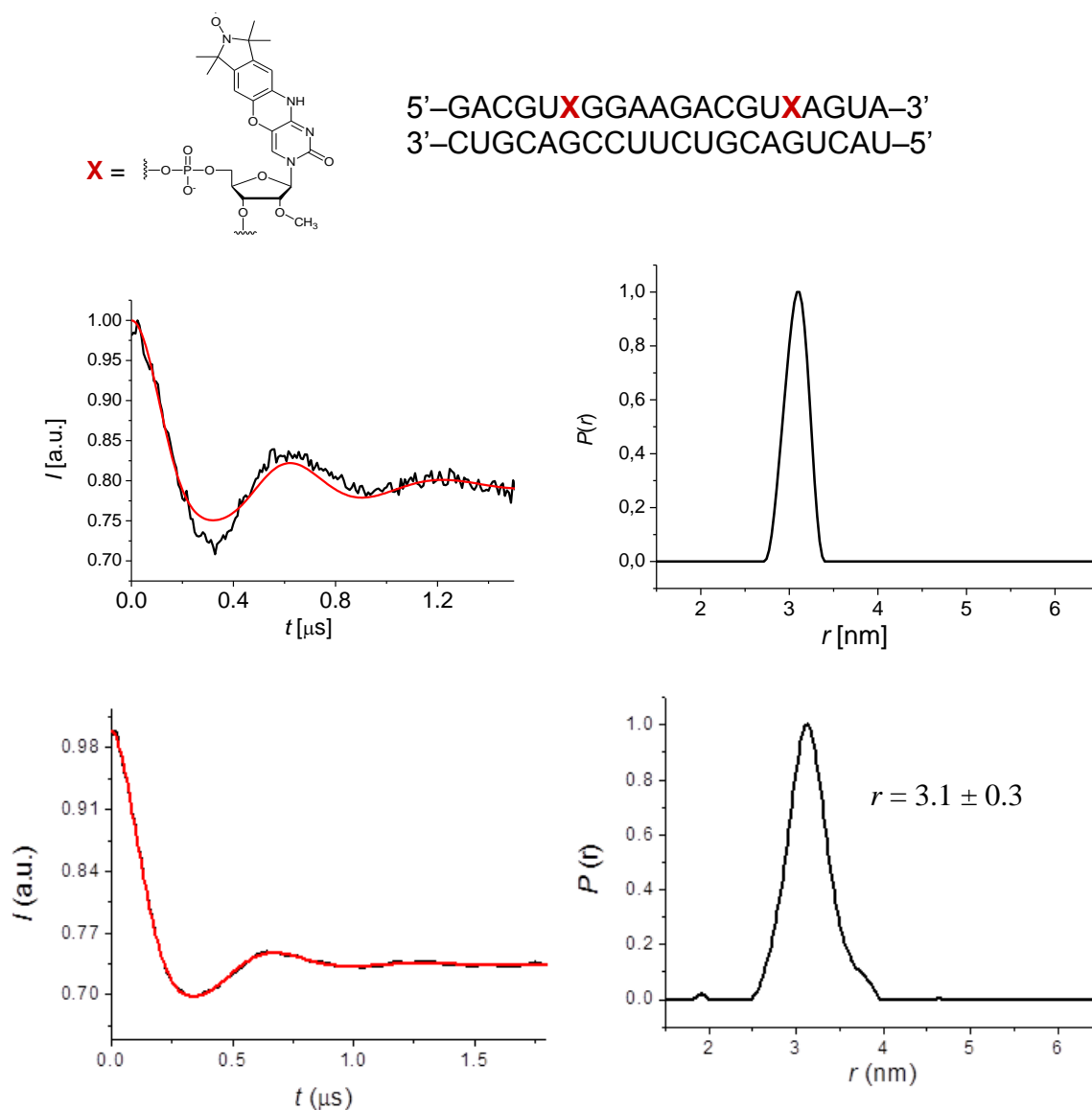
S5. Comparison of quality (*rmsd*) of the fits for fixed and variable frequency separation

S6. Summary of the structures obtained from symmetry related solutions

Supplementary Information

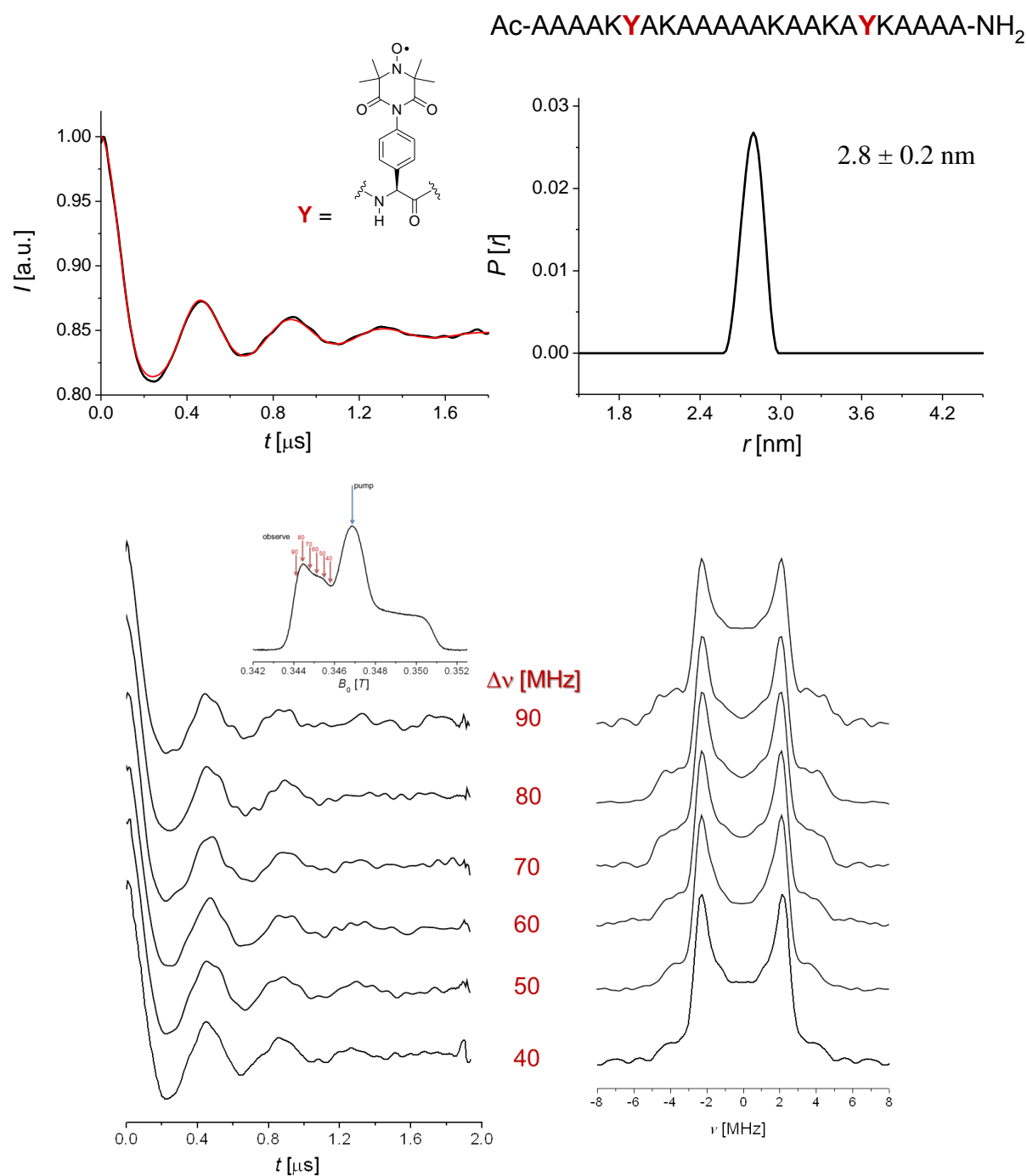
S1. PELDOR experiments at 9 GHz of RNA duplex. PELDOR traces and distance distributions (DEERAnalysis 2009, G. Jeschke *et al.* Appl. Magn. Reson. 30, **2006**, 473-498) obtained at 9 GHz on the double labeled RNA for a single trace (*top*) and after orientational averaging (sum of seven traces, *bottom*). All experiments were performed using the four-pulse PELDOR sequence. For the top trace, the pump pulse at microwave frequency ν_2 was placed on the maximum of the nitroxide spectrum with an offset of 70 MHz from the detection pulse. For orientational averaging, $\Delta\nu$ was fixed at 70 MHz and the detection position was varied over the EPR spectrum. T = 40-50 K; $\pi/2 = 16$ ns, $\pi_{\text{PELDOR}} = 36$ ns, SRT = 10 ms; 100 scans; [C] = 50-75 μM .

Figure S1



S2. 9-GHz PELDOR traces of the TOPP-labeled peptide and corresponding Fourier transformations and fit of one trace using Tikhonov regularization (DEERAnalysis 2009) showing absence of orientational selectivity at any of these pump and excitation positions. *Inset:* Echo-detected 9 GHz EPR spectrum of labeled peptide at 50 K with the excitation positions (pump) and the detection position (observe). Arrows indicate observer pulse positions varying from $\Delta\nu=40$ to 90 MHz.

Figure S2



S3. Data Analysis

Spectral analysis was performed on a series of PELDOR data acquired at detection and excitation positions across the EPR line, as specified for each experiment. Each time trace was first processed by eliminating the background decay by fitting the last two-third of the trace with an exponential or a polynomial function and dividing the experimental data by the fitted function. The modulation depth, λ , was accounted for as described in ref. 5, i.e. for each PELDOR trace i the factor $(1 - \lambda_i)$ was subtracted from the trace so that the functional form of the trace containing N contributing bi-radicals, as described by eq. 1 (main text) for one isolated bi-radical, resulted in:

$$V_i(t) = \sum_N \Psi_N \cdot \cos \omega_d (1 - 3 \cos^2 \theta_{dd}) t$$

with ω_d and θ_{dd} as given in the main text and Ψ as the probability to pump and detect the two spins belonging to a pair for each detected bi-radical. The observed modulation depth λ_i of each experimental trace corresponds to the sum of the Ψ_N for that trace. Subsequently, the amplitudes of the experimental traces were scaled with respect to the trace with maximum modulation depth, λ_{\max} (see experimental plots Fig.4).

Fit of the data was performed by non-linear least square analysis using a home-written MATLAB program with the function *fmincon* (The Mathworks, Inc.) and a minimization toolbox using Globalsearch solver. Three algorithms implemented in *fmincon*, i.e. 1) interior-point, 2) sequential quadratic programming (*sqp*), and 3) active-set, were tested for the optimization. The parameters obtained from the *sqp* algorithm provided an optimal calculation time. Therefore, the *sqp* algorithm was used for the fitting of all sets of data. The root-mean square deviation between the experiment and fitted data was calculated over all traces within one series of experiment. The fitting procedure for one set of data (typically 10-15 time traces) takes about 30-40 hours on a DELL[®] workstation (Precision T7500) with 12-core processors (3.46 GHz clock frequency).

The computation of the orientationally selected PELDOR traces consisted mainly of two steps: 1) computation of the resonance frequencies of spin 1 and spin 2 and of their dipolar frequency $D = \omega_d (1 - 3 \cos^2 \theta_{dd})$ as a function of their molecular orientations in the magnetic field; 2) computation of the probability Ψ_N that the orientations excited by pump and detection pulses belong to the same radical pair.

The angular dependent resonance field positions for spin 1 and spin 2 of the bi-radical were calculated in the high-field approximation using hyperfine and g tensors that were satisfying

the 94 GHz EPR spectra. The effect of nuclear level mixing around the x and y orientations was neglected for orientation selection. The expression for the EPR resonances is described in equation:

$$h\nu = B_0\mu_B g(\theta, \varphi) + m_I a(\theta, \varphi) \quad (1)$$

where B_0 is the magnetic field at detection, μ_B is the Bohr magneton, m_I is the nuclear spin quantum number, and g and a are the orientation dependent g and hyperfine constants, respectively. In the high-field approximation, only the z -components of the electron and nuclear spin operators, S_z and I_z , are taken into account and g and a are given respectively by the g_{zz} and A_{zz} components of the dipolar and hyperfine tensors, expressed through appropriate transformations into the laboratory frame. These transformations for the detected spin (denoted as 1) and the pumped spin (denoted as 2) were introduced as following:

$$\tilde{g}(1) = \mathbf{R}(\theta, \varphi) \mathbf{g}(1) \mathbf{R}^T(\theta, \varphi) \quad (2)$$

$$\tilde{g}(2) = \mathbf{R}(\theta, \varphi) \mathbf{R}_d \mathbf{R}'_d \mathbf{g}(2) \mathbf{R}'_d{}^T \mathbf{R}_d{}^T \mathbf{R}^T(\theta, \varphi) \quad (3)$$

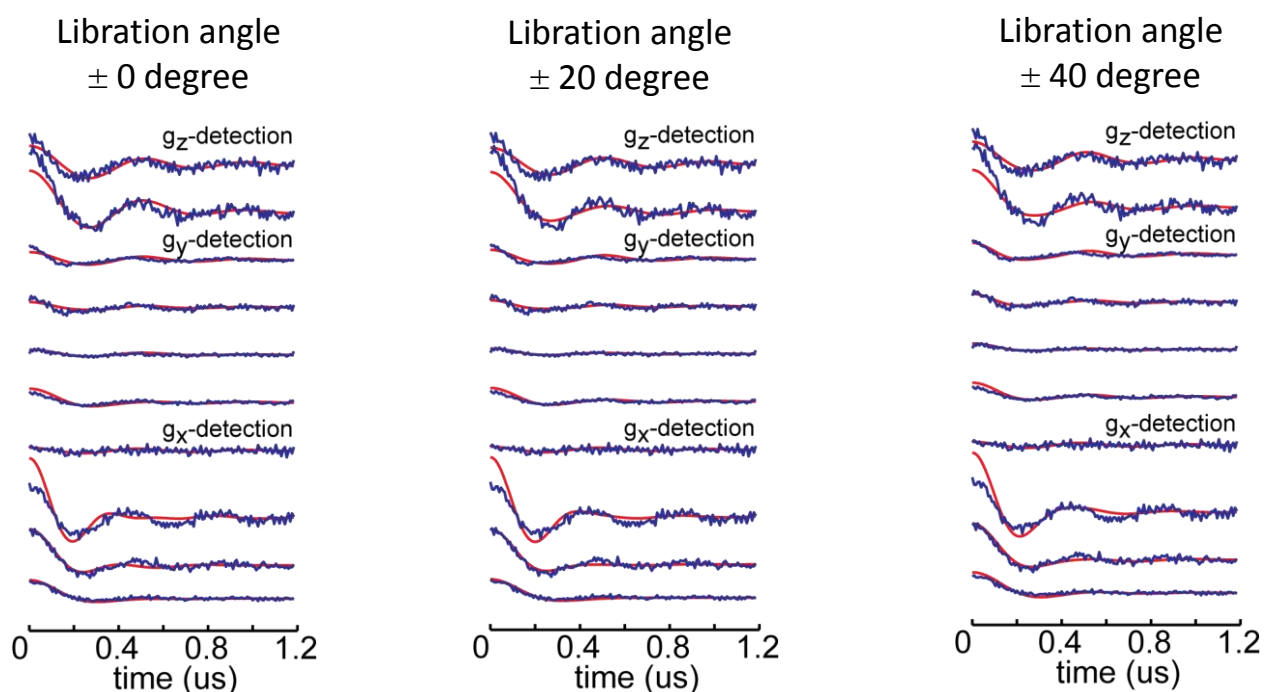
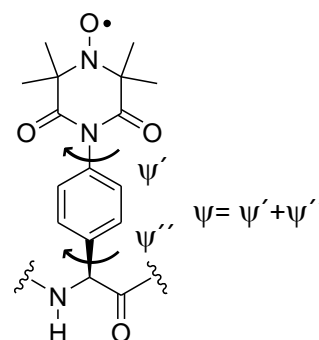
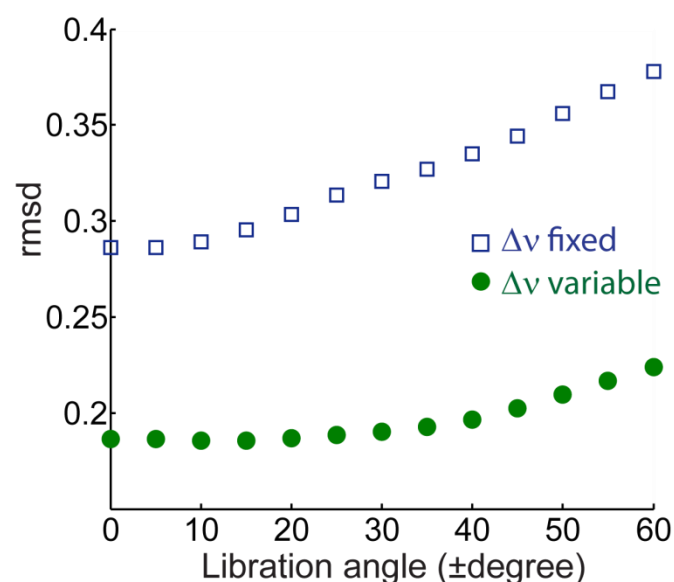
Here \tilde{g} denotes the g -tensor in the laboratory frame, \mathbf{R} and \mathbf{R}^T are Euler rotation matrices and their transposed. $\mathbf{R}(\theta, \varphi)$ describes the rotation from the $\mathbf{g}(1)$ -tensor principal axis system to the laboratory frame, \mathbf{R}_d the rotation from the dipolar tensor principal axis system into the $\mathbf{g}(1)$ -tensor and \mathbf{R}'_d from the $\mathbf{g}(2)$ -tensor principal axis system to the dipolar tensor. Similar transformations, as given in equation (2) and (3), were applied to all hyperfine tensors and to the dipolar tensor. The transformations \mathbf{R}_d and \mathbf{R}'_d contain the five Euler angles used as parameters to define the bi-radical structure as given in Scheme 1 of the main text. The transformations used here have the advantage that the resonances of the two radicals are defined with respect to the dipolar axis. Within this definition, the effect of a symmetry operation on one radical (either 1 or 2) affects only one of the two transformations \mathbf{R}_d or \mathbf{R}'_d and is easily implemented.

PELDOR frequencies were calculated as a function of the selected orientations (θ, φ) at the resonance fields of pump and detection. The angular orientations were selected by calculating the excitation profiles of pump and detection pulses and numerically collecting all angles that fall within this excitation range during the powder average over the angles θ and φ . For simplicity, no additional inhomogeneous broadening function in the EPR spectrum was accounted in the orientation selection. The excitation profiles were approximated by

Lorentzian functions that were proposed to better include effects of spectral diffusion caused by pulses in inhomogeneously broadened lines (A. Grupp & M. Mehring, in *Modern Pulsed and CW Electron Spin Resonance*, eds Kevan & Bowmann, p. 195). We note that pump and probe pulses might have small but significantly different excitation bandwidths (for same π pulse length) but this was neglected as a first approach. Whether this approximation might affect the quality of the fit for some systems remains to be checked. We also tested Gaussian functions for comparison but the quality of the fits was overall worse. A similar procedure had been employed in the past for the computation of orientation selected ENDOR spectra at high magnetic fields (Bennati et al., *J. Magn. Reson.* 1999, 138, 232-243) and had led to satisfactory results. The $\Delta\nu_{\text{exc}}$ (width of the Lorentzian excitation profile) was taken approximately as $1/t_p$, where t_p was the length of the π -pulses used for pump and detection, respectively. Finally, the probability Ψ_N was computed as a function of θ and φ and of the Euler angles defining the bi-radical structure as: $\Psi_N = \Psi_{12} + \Psi_{21}$ and $\Psi_{12} = I(\nu_{\text{d, spin 1}}) * I(\nu_{\text{p, spin 2}})$, where $I(\nu)$ are the Lorentzian functions centered at the frequency of detection (ν_{d}) and pump (ν_{p}). The index '12' stays for spin 1 being detected and spin 2 pumped and vice versa for the index '21'. Effects of overlapping pulses were neglected due to the frequency separations used in our experiments.

S4. *Effect of libration of the TOPP label around its internal axes.* In order to consider possible rotations of the TOPP labels around their internal axes interconnecting C_α with the phenyl ring and further the phenyl ring with the nitrogen of the nitroxide ring (see TOPP structure below), the time traces were simulated as a function of a libration angle ψ using the quintuplets of Euler angles in Table 1 (main text) as starting point for $\psi = 0$. The angle ψ given in the graph below represents the maximal value for a libration. The calculated traces resulted as sum of conformations for ψ being incremented linearly from zero up to the end value in steps of about 10% of the final value. The procedure was applied for label 1 and 2 simultaneously. The computed traces of all conformations were added up and gave the *rmsd* plotted below. The plot shows that the *rmsd* is not sensitive to this angle up to distributions of about 20° .

Figure S4

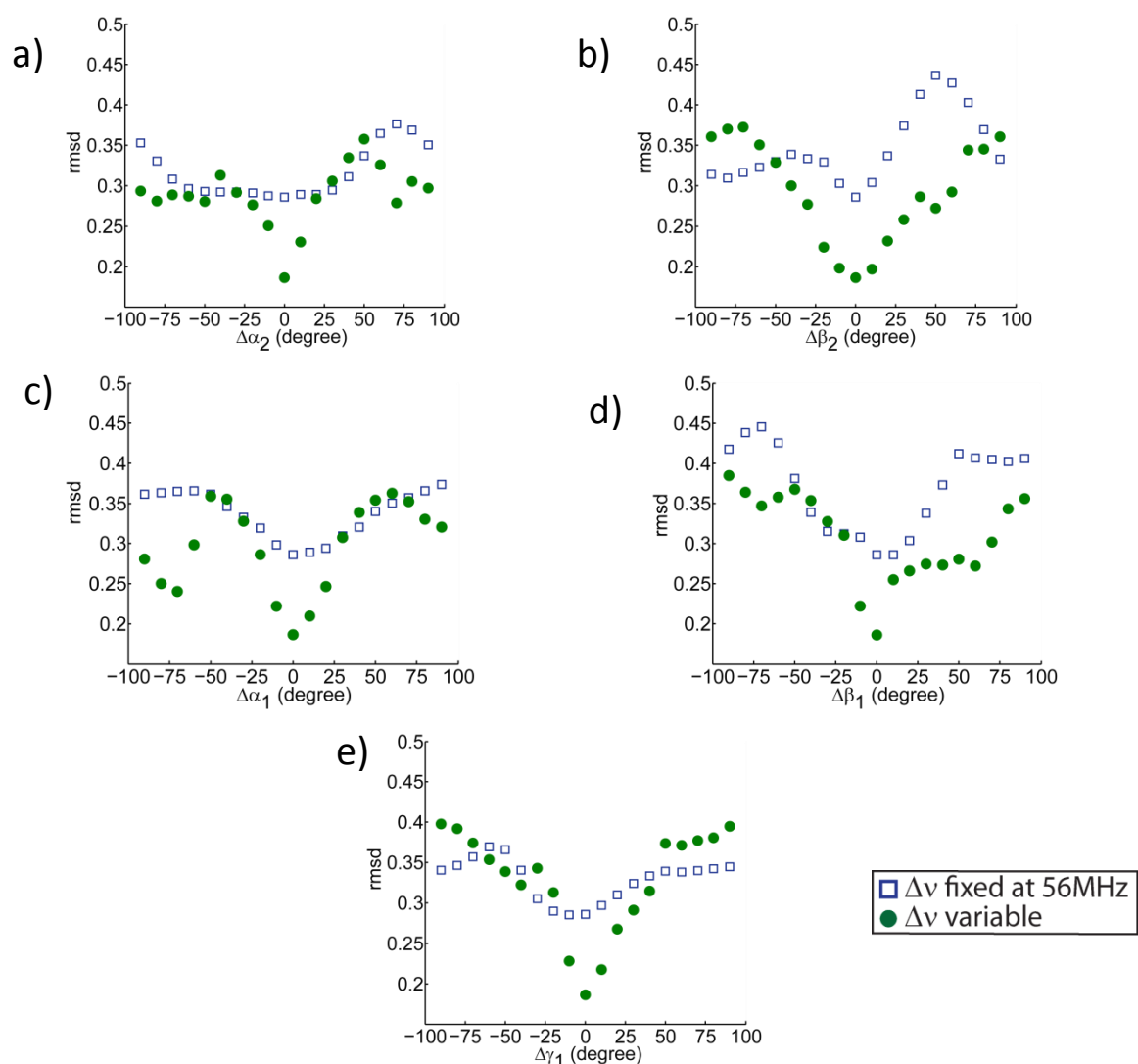


S5. Comparison of quality (*rmsd*) of the fits for fixed and variable frequency separation. To compare the quality of the fits between the two sets of experiments (fixed and variable frequency separation) the *rmsd* was calculated by varying the Euler angles one by one between -100° to $+100^\circ$ around the optimized value and keeping all other angles fixed. The optimized Euler angles ($\alpha_1, \beta_1, \gamma_1, \alpha_2$, and β_2) resulted from the fits and are taken from Table 1 in the main text.

Peptide Structure:

Plots of *rmsd* as a function of $\Delta\alpha_2, \Delta\beta_2, \Delta\gamma_1, \Delta\alpha_1$, and $\Delta\beta_1$ for the peptide structure are shown in Figure S7a, where $\Delta\alpha_2, \Delta\beta_2, \Delta\gamma_1, \Delta\alpha_1$, and $\Delta\beta_1$ are the deviation of the angles from optimized values.

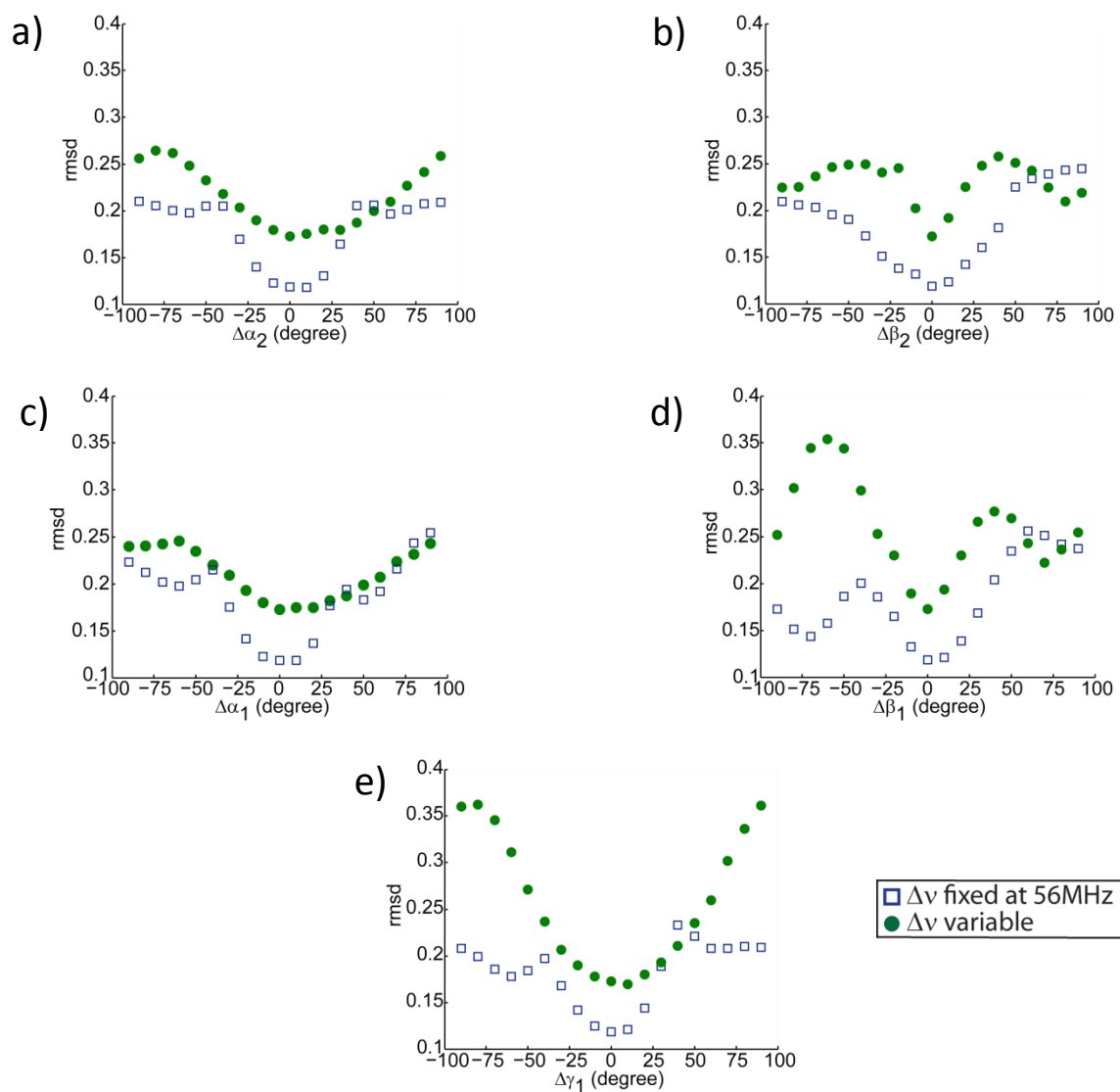
Figure S5a



RNA duplex:

Plots of *rmsd* as a function of $\Delta\alpha_1$, $\Delta\beta_1$, $\Delta\gamma_1$, $\Delta\alpha_2$, and $\Delta\beta_2$ for the RNA duplex are shown in Figure S5b.

Figure S5b



S6. Bi-radical structures from symmetry-related solutions. In this section we report the procedure employed to obtain symmetry-related bi-radical structures for the RNA duplex and the helical peptide. The solutions from the fits used as starting points were reported in Table 1 of the main text and are summarized again in Table S6a for better clarity.

Table S6a Summary of the Euler angles obtained from the data fits according to Table 1 main text.

| | Solution 2 (Δv fixed) | Solution 1 (Δv variable) |
|---|---|---|
| RNA duplex ($\alpha_1, \beta_1, \gamma_1; \alpha_2, \beta_2, 0$) ξ, β' rmsd | (123, 37, -58; 31, 13, 0) 95, 32 0.12 | (13, -32, -1; 66, -11, 0) 82, 43 0.17 |
| Peptide ($\alpha_1, \beta_1, \gamma_1; \alpha_2, \beta_2, 0$) ξ, β' rmsd | not considered | (57, -82, 32; 76, -67, 0) 128, 116 0.19 |

To examine the effect of the *directions* of the g tensor principal axes on the obtained solutions, we applied possible symmetry operations that invert the direction of the g-tensor axes of label 1 and 2 from positive to negative in the bi-radical. Only symmetry operations are allowed, which do not change the resonances of either one of the two radicals. This is accomplished by 180° rotations around one of the g axes. For instance, a 180° rotation of the label around the N-O axis (g_x axis) will swap the directions of the y and z-axes. If combinations of simultaneous rotation of both radicals were considered, 4 axes (two for each radical) were inverted at a time. It becomes clear that each change in direction of the g tensor axes involves a change in the Euler angles defining the bi-radical structure. However, we found that all of these bi-radical structures provide identical dipolar traces. As most important point, although the ambiguity derives from the form of the Hamiltonian, the label is usually attached to a bio-molecule in an asymmetric chemical environment. Thus, the symmetry-related solutions correspond to 3D bi-radical structures that are distinguishable through their chemical environment.

To obtain all symmetry-related structures, rotation operations were performed for label 1 and 2 first independently and then as possible combinations (i.e. rotation of label 1 around g_x concomitant with rotation of label 2 around g_x etc.). Following this procedure one can perform a total of 15 different operations on the two labels, in which the direction of the g-tensor principal axes become inverted. These operations were applied to the solution from the

fit, as listed in Tables S6b-d. In Tables S6b-d, the second column denotes the axis of the 180° rotation referred to the g-tensor principal axis system. The index 1 or 2 denotes the spin label, to which the operation was applied.

Bi-radical structures obtained from the 16 symmetry-related solutions are shown in Fig. S6b-d and numbered according to Tables S6b-d. The bi-radical structures were incorporated into the Pymol structures of RNA and helical peptide by first fixing the coordinates of either label 1 or label 2 in the Pymol structure and then reconstructing the coordinate of the second label according to the considered solution. The procedure was carried out for both labels as they are not distinguishable. It is evident from the obtained figures that most of the symmetry-related solutions can be discarded after evaluation of their compatibility with the expected structure.

RNA duplex:

Table S6b: Symmetry-related solutions from fits of the data with variable $\Delta\nu$ (Solution 1, Table S6)

| | Rotation | $\alpha_1 \beta_1 \gamma_1; \alpha_2 \beta_2 \gamma_2$ | ξ (NO-NO angle) | β' (plane angle) |
|----|----------------------------|--|---------------------|------------------------|
| 1 | fit result | 13 -32 -1; 66 -11 0 | 82 | 43 |
| 2 | Rot(x_1) | 13 148 -179; 66 -11 0 | 82 | 137 |
| 3 | Rot(y_1) | 13 148 1; 66 -11 0 | 98 | 137 |
| 4 | Rot(z_1) | -167 32 -1; 66 -11 0 | 98 | 43 |
| 5 | Rot(x_2) | 13 -32 -1; 114 169 0 | 82 | 137 |
| 6 | Rot(y_2) | 13 -32 -1; -66 169 0 | 98 | 137 |
| 7 | Rot(z_2) | 13 -32 -1; -114 -11 0 | 98 | 43 |
| 8 | Rot(x_1), Rot(x_2) | 13 148 -179; 114 169 0 | 82 | 43 |
| 9 | Rot(x_1), Rot(y_2) | 13 148 -179; -66 169 0 | 98 | 43 |
| 10 | Rot(x_1), Rot(z_2) | 13 148 -179; -114 -11 0 | 98 | 137 |
| 11 | Rot(y_1), Rot(x_2) | 13 148 1; 114 169 0 | 98 | 43 |
| 12 | Rot(y_1), Rot(y_2) | 13 148 1; -66 169 0 | 82 | 43 |
| 13 | Rot(y_1), Rot(z_2) | 13 148 1; -114 -11 0 | 82 | 137 |
| 14 | Rot(z_1), Rot(x_2) | -167 32 -1; 114 169 0 | 98 | 137 |
| 15 | Rot(z_1), Rot(y_2) | -167 32 -1; -66 169 0 | 82 | 137 |
| 16 | Rot(z_1), Rot(z_2) | -167 32 -1; -114 -11 0 | 82 | 43 |

Figure S6b: Plots of symmetry-related bi-radicals structures for the 16 solutions of Table S6b starting from the coordinates of label 2 (left) and of label 1 (right). Only the bi-radical structures numbered 6 and 9 of the right figure are compatible with the Pymol structure for A-form RNA. On the other hand, no solution starting from the coordinates of label 2 (left) is compatible.

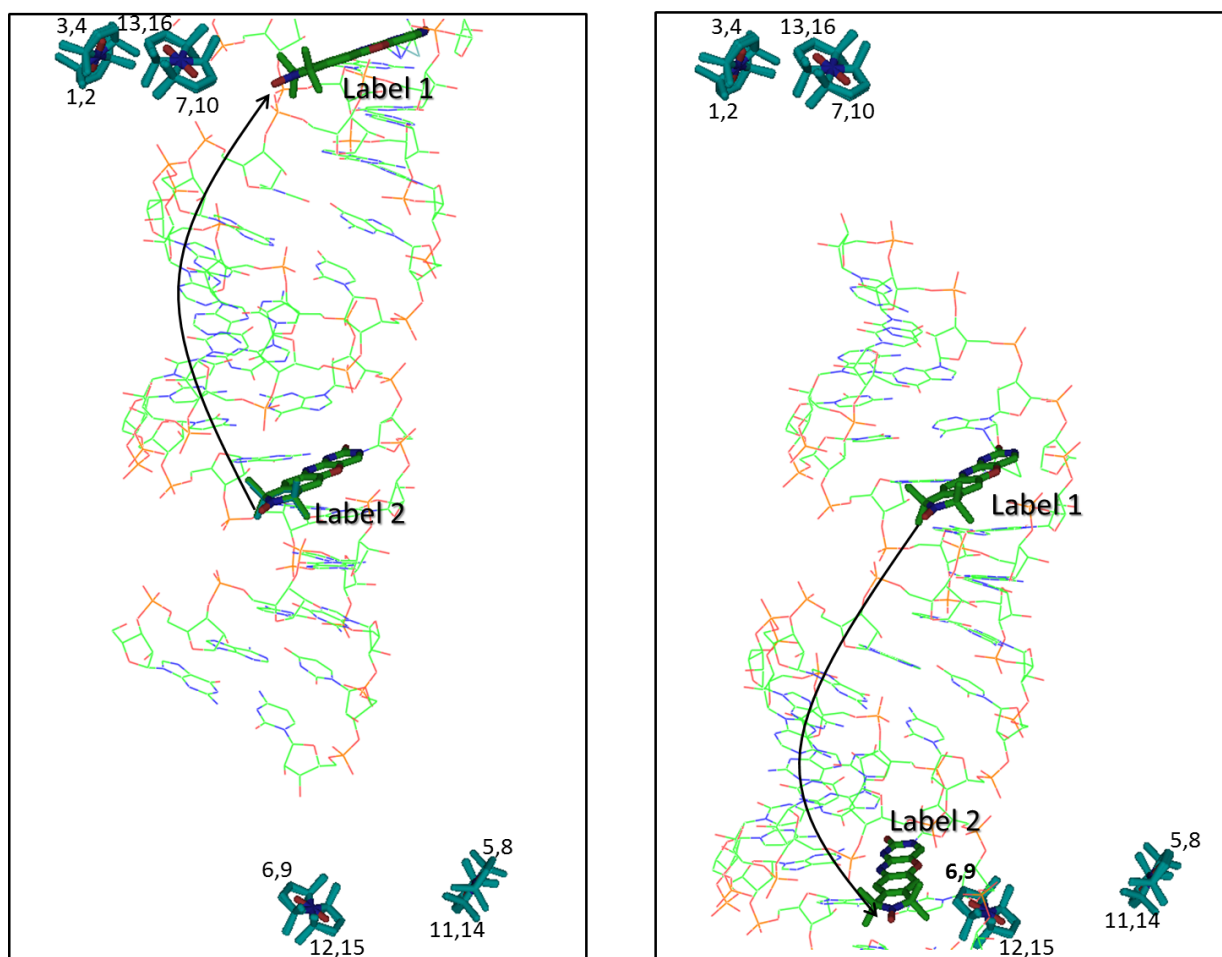
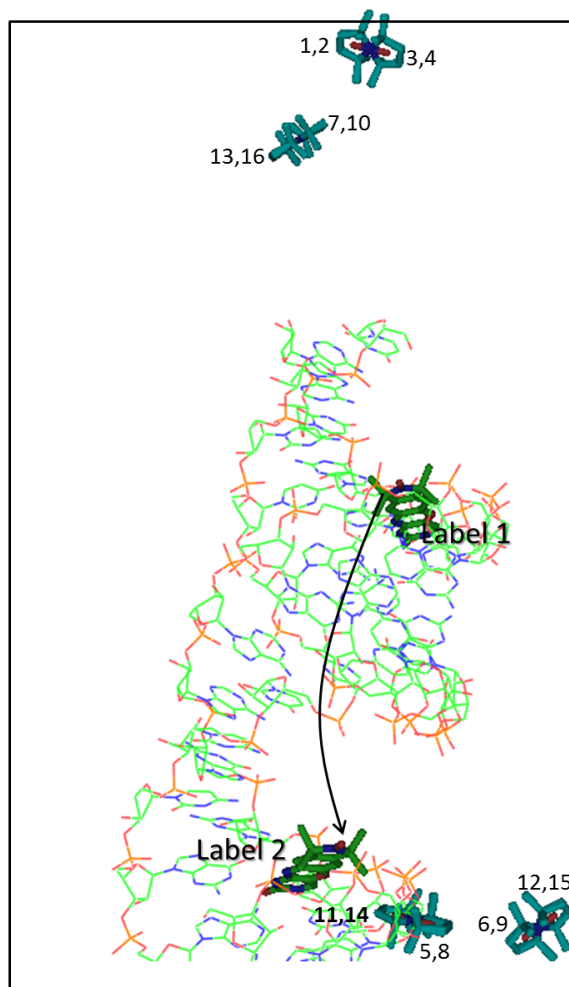
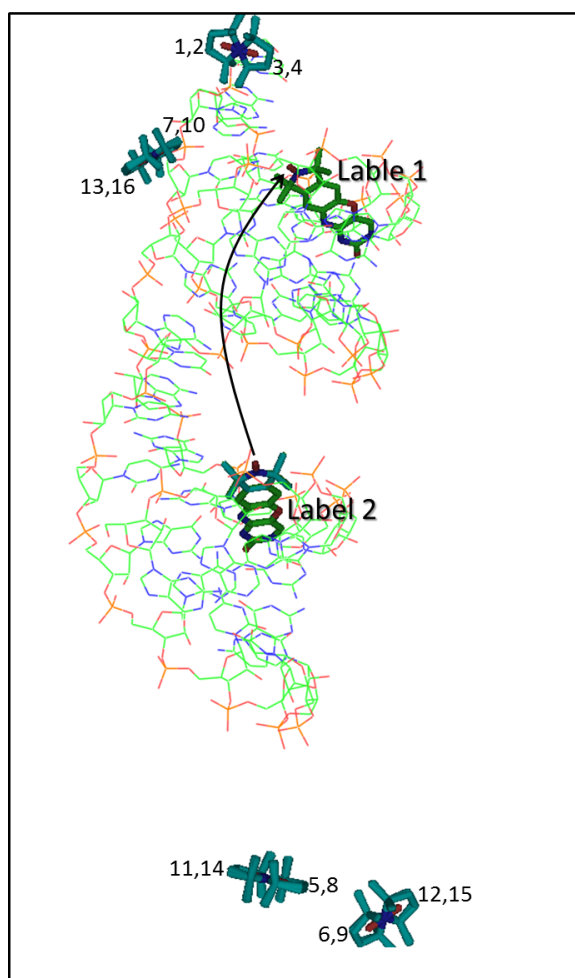


Table S6c: Symmetry-related solutions from best-fit of the data with fixed $\Delta\nu$ (Solution 2, Table S6)

| | Rotation | $\alpha_1 \beta_1 \gamma_1; \alpha_2 \beta_2 \gamma_2$ | ξ (NO-NO angle) | β' (plane angle) |
|----|----------------------------|--|---------------------|------------------------|
| 1 | fit result | 123 37 -58; 31 13 0 | 95 | 32 |
| 2 | Rot(x_1) | -57 143 58; 31 13 0 | 95 | 148 |
| 3 | Rot(y_1) | -57 143 -122; 31 13 0 | 85 | 148 |
| 4 | Rot(z_1) | 123 37 122; 31 13 0 | 85 | 32 |
| 5 | Rot(x_2) | 123 37 -58; -211 -167 0 | 95 | 148 |
| 6 | Rot(y_2) | 123 37 -58; -31 -167 0 | 85 | 148 |
| 7 | Rot(z_2) | 123 37 -58; -149 13 0 | 85 | 32 |
| 8 | Rot(x_1), Rot(x_2) | -57 143 58; -211 -167 0 | 95 | 32 |
| 9 | Rot(x_1), Rot(y_2) | -57 143 58; -31 -167 0 | 85 | 32 |
| 10 | Rot(x_1), Rot(z_2) | -57 143 58; -149 13 0 | 85 | 148 |
| 11 | Rot(y_1), Rot(x_2) | -57 143 -122; -211 -167 0 | 85 | 32 |
| 12 | Rot(y_1), Rot(y_2) | -57 143 -122; -31 -167 0 | 95 | 32 |
| 13 | Rot(y_1), Rot(z_2) | -57 143 -122; -149 13 0 | 95 | 148 |
| 14 | Rot(z_1), Rot(x_2) | 123 37 122; -211 -167 0 | 85 | 148 |
| 15 | Rot(z_1), Rot(y_2) | 123 37 122; -31 -167 0 | 95 | 148 |
| 16 | Rot(z_1), Rot(z_2) | 123 37 122; -149 13 0 | 95 | 32 |

Figure S6c: Plots of symmetry-related bi-radical structures for the 16 solutions of Table S6c

The biradical structures numbered 11 and 14 of the right figure are compatible with the Pymol structure for A-form RNA. On the other hand, no solution starting from the coordinates of label 2 (left) is compatible.



Peptide:

Table S6d: Symmetry-related solutions from best-fit of the data with variable $\Delta\nu$ (entry second row, second column Table S6)

| | Rotation | $\alpha_1 \beta_1 \gamma_1; \alpha_2 \beta_2 \gamma_2$ | ξ (NO-NO angle) | β' (plane angle) |
|----|----------------------------|--|---------------------|------------------------|
| 1 | fit result | 57 -82 32; 76 -67 0 | 128 | 116 |
| 2 | Rot(x_1) | 57 98 148; 76 -67 0 | 128 | 64 |
| 3 | Rot(y_1) | 57 98 -32; 76 -67 0 | 52 | 64 |
| 4 | Rot(z_1) | -123 82 32; 76 -67 0 | 52 | 116 |
| 5 | Rot(x_2) | 57 -82 32; 104 113 0 | 128 | 64 |
| 6 | Rot(y_2) | 57 -82 32; -76 113 0 | 52 | 64 |
| 7 | Rot(z_2) | 57 -82 32; -104 -67 0 | 52 | 116 |
| 8 | Rot(x_1), Rot(x_2) | 57 98 148; 104 113 0 | 128 | 116 |
| 9 | Rot(x_1), Rot(y_2) | 57 98 148; -76 113 0 | 52 | 116 |
| 10 | Rot(x_1), Rot(z_2) | 57 98 148; -104 -67 0 | 52 | 64 |
| 11 | Rot(y_1), Rot(x_2) | 57 98 -32; 104 113 0 | 52 | 116 |
| 12 | Rot(y_1), Rot(y_2) | 57 98 -32; -76 113 0 | 128 | 116 |
| 13 | Rot(y_1), Rot(z_2) | 57 98 -32; -104 -67 0 | 128 | 64 |
| 14 | Rot(z_1), Rot(x_2) | -123 82 32; 104 113 0 | 52 | 64 |
| 15 | Rot(z_1), Rot(y_2) | -123 82 32; -76 113 0 | 128 | 64 |
| 16 | Rot(z_1), Rot(z_2) | -123 82 32; -104 -67 0 | 128 | 116 |

Figure S6d: Plots of symmetry-related bi-radical structures for the 16 solutions of Table S6d. The bi-radical structures obtained in the left panel, labeled 1 and 2 are compatible with a α -helix structure of the peptide, as shown in main text. On the other hand, no solution starting from the coordinates of label 1 (right) is compatible.

